On the Representation of Convectively Coupled Kelvin Waves in Operational Forecast Models: An Object-Tracking Perspective

QUINTON A. LAWTON,[a] ROSIMAR RIOS-BERRIOS,[a] FALKO JUDT,[a] LINUS MAGNUSSON,[b] AND MARTIN KÖHLER[c]

[a] NSF National Center for Atmospheric Research, Boulder, Colorado
[b] ECMWF, Reading, United Kingdom
[c] Deutscher Wetterdienst, Offenbach, Germany

(Manuscript received 2 September 2025, in final form 19 March 2026, accepted 6 April 2026)

ABSTRACT: Accurately forecasting convectively coupled Kelvin waves (CCKWs) remains a major challenge, as many models struggle to realistically simulate their structure and propagation. However, previous studies have often focused on a limited set of models or relied on diagnostics that obscure individual wave characteristics. It also remains unclear how well models represent interactions between CCKWs and other tropical waves, such as easterly waves (EWs). In this study, an object-based tracking framework is used to evaluate forecasts of CCKWs and EWs across nine operational models. These include traditional physics-based models and ECMWF's new Artificial Intelligence Forecasting System (AIFS). Forecast skill is assessed as a function of observed wave attributes, life cycle phase, and environmental context. All nine models are found to underestimate CCKW strength and misrepresent the vertical structure, with the largest errors occurring during wave growth. More skillful models exhibit better vertical coherence between Kelvin wave–filtered rainfall and divergence, suggesting that forecast errors are linked to deficiencies in representing convective coupling. Forecast models also frequently miss CCKW–EW interactions, and captured interactions are typically understrengthened. Despite these challenges, AIFS forecasts of EWs and CCKWs compare favorably to those of physics-based models. While the original analysis period overlaps the AIFS training window, we find that this skill persists for forecasts outside that period, highlighting the potential of data-driven systems for tropical wave prediction. These results underscore persistent challenges in CCKW forecasting and motivate further work to better understand the representation of tropical wave interactions in numerical models.

SIGNIFICANCE STATEMENT: Waves in the tropical atmosphere, including convectively coupled Kelvin waves (CCKWs), play a key role in shaping local weather. While previous studies have shown that CCKWs are hard to forecast, most have used a limited range of models and have not directly tracked individual waves. Here, we use a wave-following framework to evaluate how well nine different weather models forecast CCKWs. All models underestimate CCKW strength, especially during growth stages, and poorly represent interactions between CCKWs and easterly waves. Better-performing models show a stronger connection between the CCKW's convection and atmospheric circulation ("convective coupling"). These results highlight that persistent shortcomings in representing CCKWs are tied to convective coupling and suggest these errors may affect high-impact weather forecasts.

KEYWORDS: Kelvin waves; Atmospheric waves; Model comparison; Model evaluation/performance; Numerical weather prediction/forecasting

1. Introduction

Weather in the tropics is strongly influenced by atmospheric waves. Among these, convectively coupled Kelvin waves (CCKWs) and easterly waves (EWs) have received considerable attention. CCKWs are eastward-propagating equatorial waves with wavelengths that generally span 3000–7000 km and typical phase speeds of 10–20 m s^{-1} (Yang et al. 2007a, 2009; Kiladis et al. 2009; Dias and Pauluis 2011). Although they share structural similarities with the dry Kelvin waves described by linear theory (Matsuno 1966), CCKWs are coupled to moist convection, which alters their dynamics and influence on the tropical atmosphere (Kiladis et al. 2009; Herman et al. 2016; Wolding et al. 2020a,b). While CCKW dynamics are largely driven by buoyancy fluctuations, convection and cloud-radiative interactions contribute significantly to wave propagation and growth (Adames et al. 2019; Mayta and Adames 2023; Rios-Berrios et al. 2023).

EWs, meanwhile, are westward-propagating off-equatorial disturbances that travel at slower phase speeds of 8–10 m s^{-1} and generally span 2000–4000 km (Reed et al. 1988; Hollis et al. 2024). While EWs exist globally, those originating over the Pacific and Africa are the most extensively studied (Burpee 1972; Hopsch et al. 2010; Torres et al. 2021; Huaman et al. 2021). Recent work has demonstrated that EWs exhibit distinct underlying dynamics and variability based on their location and climatological context (e.g., Hopsch et al. 2010; Vargas Martes et al. 2023; Lawton et al. 2025).

Supplemental information related to this paper is available at the Journals Online website: https://doi.org/10.1175/WAF-D-25-0182.s1.

Corresponding author: Quinton A. Lawton, qlawton@ucar.edu

DOI: 10.1175/WAF-D-25-0182.1

Both CCKWs and EWs can have significant impacts on regional weather patterns and extreme weather. EWs often serve as "seeds" for tropical cyclone (TC) formation, and they can contribute to extreme rainfall in regions such as the African Sahel, the Caribbean, South America, and the Maritime Continent (Moron et al. 2008; Lubis and Jacobi 2015; Engel et al. 2017; Russell et al. 2017; Dominguez et al. 2020). Similarly, CCKWs strongly influence rainfall variability and TC formation (Mounier et al. 2007; Mekonnen et al. 2008; Lubis and Jacobi 2015; Schreck 2015; Schlueter et al. 2019; Lawton and Majumdar 2023; Rios-Berrios et al. 2024). Interactions between CCKWs and EWs can also modify wave characteristics and exacerbate their impacts. For example, Lawton et al. (2022) and Lawton and Majumdar (2023) found that CCKWs alter the characteristics of African EWs and may enhance TC genesis processes. Other studies have shown that the superposition of CCKWs and EWs can increase the probability of extreme rainfall events (e.g., Ferrett et al. 2020; Latos et al. 2021; Peyrillé et al. 2023).

Given their large-scale organization and known interactions, CCKWs have been theorized as a potential source of tropical predictability. Yet, CCKWs remain challenging to forecast. Studies have routinely found that CCKWs are poorly represented in forecast models at medium-range time scales (Dias et al. 2018; Bengtsson et al. 2019; Yang et al. 2021; Gehne et al. 2022; Lawton et al. 2024; Cruz et al. 2024) and that their predictive skill on longer subseasonal time scales is limited (Janiga et al. 2018; Schreck et al. 2020; Dias et al. 2023). Forecast skill also varies widely depending on the model and wave identification method utilized. For example, Yang et al. (2021) found skill out to 4 days using the Met Office model and a projection-based approach, while Gehne et al. (2022) reported minimal skill beyond 2 days using the GFS model and a spatiotemporal filtering technique.

A key contributor to these deficiencies appears to be cumulus parameterization (Dias et al. 2018; Bengtsson et al. 2019; Yang et al. 2021; Gehne et al. 2022; Lee et al. 2025). CCKW representation is highly sensitive to the choice of cumulus scheme, in part because of the inability of many schemes to fully represent stratiform processes (Bengtsson et al. 2019; Lee et al. 2025). Relatedly, high-resolution modeling studies have shown that explicitly resolving convection can significantly improve the representation of CCKWs and their convective coupling (Judt and Rios-Berrios 2021; Weber et al. 2021; Rios-Berrios et al. 2023). However, it is unlikely that cumulus parameterizations are the only factor in CCKW performance. Work by Bengtsson et al. (2019) noted differences in the planetary boundary layer that could not be attributed back to the convective scheme. In simulations of a strong CCKW event, Lawton et al. (2024) found that neither increasing the horizontal grid spacing to convective-permitting (3 km) resolutions nor perturbing the initial CCKW signals resulted in an appreciable increase in model performance. These and other results (e.g., Yang et al. 2021; Cruz et al. 2024) suggest that additional factors, such as attributes of the CCKW itself or the model's initialization fields, could be responsible for deficiencies in resolving some CCKWs.

These studies suggest that CCKW predictability may be influenced by intrinsic wave properties and the wave's surrounding environment. However, most previous work has focused on a limited number of models or isolated case studies, often relying on regression-based techniques or spatiotemporal filtering to identify waves (e.g., Dias et al. 2018; Bengtsson et al. 2019; Yang et al. 2021; Gehne et al. 2022; Lawton et al. 2024). While these methods have yielded valuable insights, they offer limited ability to isolate how specific wave or environmental characteristics contribute to forecast error. Inconsistencies in wave identification techniques across studies further hinder cross-model comparisons and the development of broader conclusions about forecast biases. Furthermore, it remains unknown how well models represent interactions between CCKWs and other disturbances, such as EWs. These limitations highlight the need for a more systematic assessment of CCKW forecast performance across numerical models.

Recently updated tools and datasets offer new opportunities to address this gap. The first is the expanded use of object tracking to quantify waves and disturbances. While such methods have long been used for TC identification in observations and numerical models (e.g., Ryglicki and Hart 2015), their application has recently expanded to include EWs (Bain et al. 2014; Brammer and Thorncroft 2015; Elless and Torn 2018; Lawton et al. 2022; Hollis et al. 2024). Another important development is the Different Models, Same Initial Conditions (DIMOSIC) project, which produced a suite of operational models with identical initial conditions over a full year (Magnusson et al. 2022). This dataset provides an opportunity to assess tropical wave forecast performance and sources of error across many different modeling systems, while removing initialization differences as a major factor in how models represent CCKWs.

There is also a need to understand how tropical waves are represented in new artificial intelligence (AI) modeling systems. These systems use machine learning algorithms trained on years of meteorological data to generate forecasts. Many AI-based systems are now matching or even outperforming physics-driven numerical weather prediction systems in traditional metrics (Pathak et al. 2022; Lam et al. 2023; Lang et al. 2024a). Recently, the European Centre for Medium-Range Weather Forecasts (ECMWF) made operational their own AI weather model, the AI Forecasting System (AIFS; Lang et al. 2024b,a). Although these systems are often evaluated using standard metrics such as surface temperature or geopotential height, it remains unclear how well they capture tropical waves.

In this paper, we address outstanding gaps in tropical wave forecasting by applying an object-tracking framework to forecasts from the DIMOSIC dataset and ECMWF's AIFS system. We have three main goals: 1) to identify systemic errors in CCKW forecasts, 2) to evaluate sources of intermodel differences in CCKW representation and their implications for numerical prediction, and 3) to quantify how well CCKW–EW interactions are captured by modern forecasting systems. Our focus on CCKW–EW interactions is motivated by their growing recognition as contributors to

TABLE 1. Basic description of numerical models used in this study, adapted in part from Magnusson et al. (2022). The Met. France ARPEGE model has a variable spatial grid, with the highest resolutions centered on Europe. More information regarding the AIFS runs can be found in documentation by Mass (2024) and Lang et al. (2024b).

Abbreviation	Institute	Model	Resolution
IFS 47r1	ECMWF	Integrated Forecasting System (IFS; v47r1)	9 km/137 levels
IFS 47r3	ECMWF	Integrated Forecasting System (IFS; v47r3)	15 km/80 levels
AIFS	ECMWF	Artificial Intelligence Forecasting System (AIFS; v1.0)	36 km/13 levels
ICON	DWD	Icosahedral Nonhydrostatic Model (ICON; April 2021)	13 km/90 levels
ICON ReRun	DWD	Icosahedral Nonhydrostatic Model (ICON; version April 2025)	13 km/90 levels
UKMO	Met Office	Unified Model (UM)	10 km/70 levels
SHIELD	GFDL	System for High-Resolution Prediction on Earth-to-Local Domains (rt2019)	13 km/91 levels
CMC	CMC	Global Environmental Multiscale Model (GEM; v5.0.2)	15 km/80 levels
Met. France	Météo-France	Action de Recherche Petite Echelle Grande Echelle (ARPEGE; v46T1)	5–25 km/105 levels

extreme weather. Section 2 describes the datasets and methodology, including model specifications, wave tracking techniques, and evaluation metrics. Forecast statistics and biases are presented in section 3, followed by an analysis of potential drivers of forecast errors in section 4. Section 5 examines model skill in forecasting EWs and their interactions with CCKWs. Key findings and their implications are summarized in section 6.

2. Data and methods

We utilize a combination of reanalysis and satellite data to identify tropical waves for verification. For reanalysis data, the fifth generation ECMWF atmospheric reanalysis (ERA5) dataset was obtained from 2001 through October 2024 on a $1° \times 1°$ grid and at 6-hourly temporal resolution (Hersbach et al. 2020). We acquire 24-h estimates of observed precipitation from the final stage run of the Integrated Multi-satellitE Retrievals for GPM (IMERG) dataset, version 7 (Huffman et al. 2023), and daily mean outgoing longwave radiation (OLR) from the NOAA interpolated OLR dataset (Liebman and Smith 1996). These data are conservatively remapped to a $1° \times 1°$ grid.

a. DIMOSIC operational models

A basic summary of the operational forecast models used in this study can be found in Table 1. Most forecast data are obtained from the DIMOSIC project, in which 10-day operational forecast models were initialized using identical operational ECMWF analyzes. Simulations were produced every 3 days (at 0000 UTC) for a 1-yr period stretching from 6 June 2018 through 4 June 2019 (for more, see Magnusson et al. 2022). We also produced a new set of Icosahedral Nonhydrostatic (ICON) forecasts (which we call "ICON ReRun") using a more recent operational version of this model released in April 2025. These additional runs allow us to test whether ICON's CCKW representation is consistent across versions and to obtain specific humidity data missing from the original simulations.

We supplement the DIMOSIC dataset with corresponding hindcasts using version 1.0 of ECMWF's AIFS system (Lang et al. 2024b,a). For these model runs, we use the same input fields (IFS analysis) as the DIMOSIC models.[1] AIFS leverages a graph neural network encoder and decoder trained on ERA5 reanalysis data to produce medium-range weather forecasts. Of interest to us is how accurately the AIFS system is able to represent CCKWs and how its CCKW forecasts compare to that of the other dynamical models. One caveat is that the dates used in this study (June 2018–19) fall within the training period for the AIFS v1.0 model. While we primarily validate CCKWs using a precipitation dataset not used in this model training, improved AIFS skill in other ERA5-derived fields could still potentially inflate our calculation of CCKW forecast skill. To address this, we also supplement these runs with additional analysis outside the training period (see section 3b). Nevertheless, since our interest is determining whether AIFS is able to accurately represent and propagate tropical wave features, the 2018–19 comparison of AIFS to the DIMOSIC models still provides valuable insight.

Total precipitation was output across all included models, allowing for CCKWs to be objectively identified and tracked. However, only a limited number of other variables and six vertical levels were consistently available for all nine DIMOSIC models.

b. Identifying and tracking Kelvin waves

Equatorial wave signals can be challenging to distinguish from noise in unfiltered observational and numerical simulation data. Various wave filtering and identification methods exist, each with their own advantages and disadvantages (Knippertz et al. 2022). Here, we seek to build on these methods by systematically identifying and classifying CCKW objects from the filtered data. While object tracking has been manually applied to individual CCKW case studies (e.g., Weber et al. 2021), the scale of our analysis (122 runs across 9 forecast models) requires a more automated method.

[1] The input field requirements of AIFS differ from the other physics-driven models. AIFS requires input fields both at the time of initialization as well as 6 h before. It also requires specific pressure levels as inputs and a spatial resolution of $0.25° \times 0.25°$. It is possible these nuances could contribute to differences between the data-driven AIFS and the other physics-driven models.

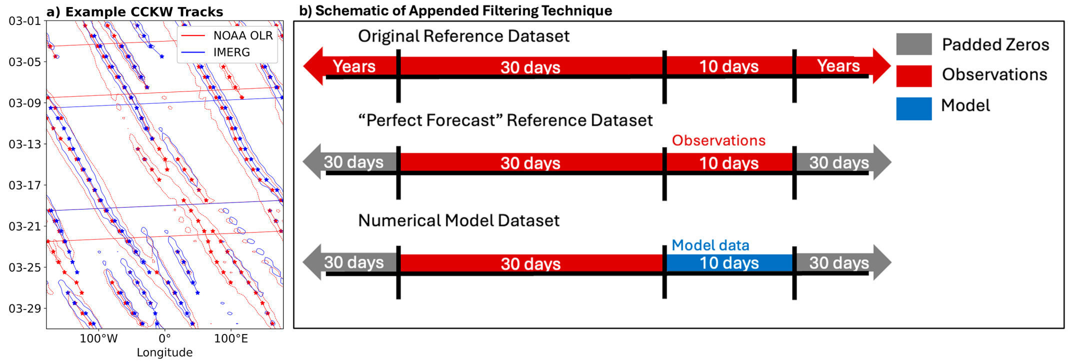

FIG. 1. (a) Hovmöller diagram showing 10°S–10°N averages of filtered IMERG (blue contours) and NOAA OLR (red contours) data for March of 2018, with contours increasing at 1.0 standard deviation intervals. An additional 0.5 standard deviation contour is included. Objective CCKW tracks are overlaid (lines with star markers). (b) Schematic illustrating how datasets are modified to ensure CCKW-filtered fields are comparable between the numerical simulations and reference data.

We first use the frequency–wavenumber filtering method of Wheeler and Kiladis (1999) to isolate Kelvin wave–like signals in daily mean precipitation or OLR. The Kelvin window is bounded by a temporal period of 2.5–20 days, a zonal wavenumber from 1 to 14, and an equivalent depth of 8–90 m. The standard deviation of these filtered fields at each grid point is computed across the full OLR and IMERG datasets and used to normalize the observed data and that from numerical simulations. We then take 10°S–10°N averages of these normalized fields.

Next, we modify the EW tracker of Lawton et al. (2022) to identify the convectively active center of CCKWs in longitude–time space, using local signal peaks. New CCKW objects are initialized if a local peak reaches one standard deviation and is not close to an existing wave object. Otherwise, these peaks are added to existing CCKW tracks if they are at least 0.25 standard deviations and within 23° of an existing wave. These thresholds were obtained after extensive sensitivity testing and are a trade-off between capturing the majority of real CCKW tracks and reducing noise.

We use this methodology to build a long-term (2001–24) climatology of CCKW tracks using Kelvin-filtered IMERG precipitation and NOAA OLR data, though only the years 2018–19 are analyzed in this study. An example of these tracks relative to the Kelvin-filtered signal is shown in Fig. 1a. In general, the objective wave tracks closely follow the filtered fields and capture most of their lifespans. Using NOAA OLR data produces additional CCKW objects compared to IMERG, but the overall findings are similar between the precipitation and OLR fields. Furthermore, the characteristics of the tracked waves are consistent with previous studies. For example, CCKW phase speeds range from 8 to 18 m s^{-1} in both IMERG and NOAA OLR datasets (not shown), in agreement with prior work (Yang et al. 2007b; Kiladis et al. 2009). Vertical composites of divergence, specific humidity, and temperature (not shown) also exhibit the canonical east-to-west tilt documented in CCKW observations (Kiladis et al. 2009; Mayta et al. 2021). Overall, these results support the robustness of the tracking methodology and its consistency with established CCKW behavior.

c. *Tracking waves in numerical simulations*

One disadvantage of spatiotemporal filtering is that it is not time independent and can produce inaccurate results for shorter datasets, such as numerical simulations (Yang et al. 2021; Knippertz et al. 2022). To address this, we compare CCKWs in numerical simulations to a reference dataset that is of the same length as the model data. A diagram illustrating this process is shown in Fig. 1b. First, we produce 24-h averages of precipitation rates and/or OLR in each numerical simulation. These data are padded with observations in the 30 days prior to model initialization, with 30 days of zeros added at either end.[2] This appended dataset is Kelvin filtered, and the CCKW tracker is applied. An identical process is then carried out on a "perfect forecast" that has had model data replaced by corresponding IMERG or OLR observations. This approach closely follows the methodology implemented by Janiga et al. (2018) and Schreck et al. (2020). An example of how tracked CCKW locations relate to spatial fields is shown in Fig. 2. CCKWs that exist in the perfect forecast dataset but not a model forecast, such as the CCKW located over the Maritime Continent in Fig. 2a, are considered missed events.

One consequence of the perfect forecast method is that it can produce multiple reference CCKWs that all correspond to a single observed CCKW event. This is because perfect forecasts are generated for each model forecast run. To resolve this, reference wave objects from the perfect forecasts are paired with their "parent" CCKW in the full observational dataset if they exist within 10° longitude of each

[2] We also tested a version of this methodology where reference data are not appended in the 30 days prior to model initialization, which yielded the same overall conclusions as the padded reference data. A relevant figure is included in the supplemental material (Fig. S3).

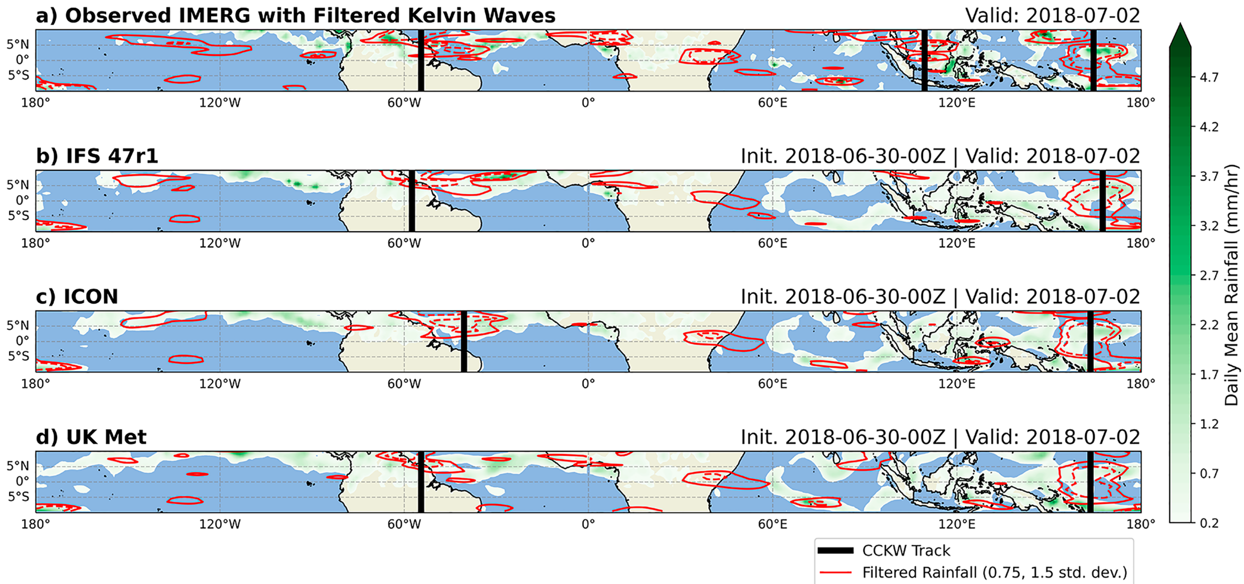

FIG. 2. Snapshot of daily mean rainfall (shading; mm h^{-1}), Kelvin-filtered rainfall (red contours, standard deviation), and tracked CCKW positions (vertical black lines) valid on 2 Jul 2018 for forecasts initialized on 30 Jun 2018. Subpanels show output from (a) the perfect forecast observations, (b) IFS 47r1, (c) ICON, and (d) Met Office models.

other at any point of their lifetime. A similar process pairs simulated CCKWs to their corresponding perfect forecasts. This hierarchy ensures that forecast metrics are computed using the perfect forecast objects while maintaining a clear link to the observed CCKW event. More details can be found in the supplemental text T1 in the online supplemental material.

Additional validation of forecast metrics was conducted using unfiltered environmental fields surrounding CCKW objects. Dataset length primarily influences the magnitude of the filtered signals as opposed to their phasing (see Fig. S2 for an example). This indicates that CCKW object tracks can reliably be used as a reference for compositing unfiltered environmental variables.

We note that other spatial projection filtering methods, such as the parabolic cylindrical function (PCF) method developed by Yang et al. (2003), are less affected by time-dependence limitations. However, the PCF method produced degraded CCKW objects that were more sensitive to high-frequency features and fragmented in time (not shown).

d. *Identifying easterly waves and interactions*

EWs are identified in the Atlantic and eastern Pacific Ocean basins using the objective wave tracker developed by Lawton et al. (2022) and updated by Lawton et al. (2025). This method uses radially averaged 700-hPa curvature vorticity to initiate and track EWs. Prior to running the tracker, the preceding week of ERA5 data is appended to each numerical simulation to allow additional spinup time. Because EWs have a coherent synoptic vorticity signature, the input data are not time filtered. This allows model EW tracks to be directly compared to the full ERA5 EW climatology published by Lawton et al. (2025). We also identify CCKW–EW wave interactions.[3] To do so, EW track data are interpolated from 6 hourly to once daily to match the temporal resolution of CCKW tracks. Then, CCKW and EW tracks are analyzed for instances of a CCKW passing an EW in longitude. This process is done for the full reference dataset, for each simulation, and for each simulation's perfect forecast observations. As with the CCKWs, forecast metrics are computed only for interactions that exist in the perfect forecast dataset. To check that differences in wave tracking methods did not influence our CCKW–EW interaction results, we also modified the CCKW wave tracker to identify EW-like objects in precipitation data filtered within the tropical depression (TD) band. As discussed later, this did not affect our final conclusions.

e. *Forecast metrics and wave diagnostics*

Following work by Elless and Torn (2018) evaluating EWs in an object-oriented framework, we diagnose each model's prediction of CCKWs and EWs by calculating forecast bias [$b(t)$] and bias-corrected root-mean-square error (RMSE). These are represented mathematically as

[3] While the word "interaction" implies a nonlinear relationship or outcome, what is being identified here is simply the time and location that tracked CCKWs and EWs pass each other in longitude. We choose to refer to these passages as interactions for simplicity and because of evidence in the literature that interactions between these two waves commonly occur (Mantripragada et al. 2021; Lawton et al. 2022; Lawton and Majumdar 2023)

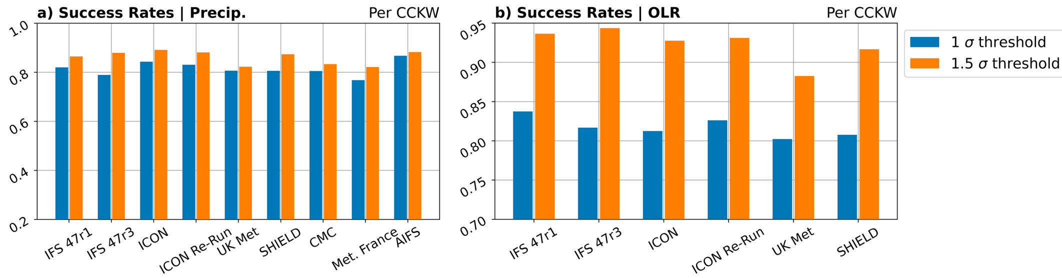

FIG. 3. Comparison of model success rates in capturing CCKWs in the (a) total precipitation tracking framework and (b) OLR tracking framework. The blue bars are success rates considering all tracked CCKWs, whereas the orange bars only include statistics for reference CCKWs that exceed a strength of 1.5 standard deviations at some point in their life cycle. Forecast statistics are only computed for CCKWs that exist in observations at the time of model initialization.

$$\mathrm{RMSE} = \sqrt{\frac{1}{M(t)} \sum_{m=1}^{M(t)} [\overline{x}_m(t) - b(t) - \overline{o}_m(t)]^2}, \qquad (1)$$

where

$$b(t) = \frac{1}{M(t)} \sum_{m=1}^{M(t)} \overline{x}_m(t) - \overline{o}_m(t), \qquad (2)$$

where m represents the model run, $\overline{x}_m(t)$ is a forecast value at a given lead time t, $\overline{o}_m(t)$ is a corresponding reference value from ERA5 or IMERG, $b(t)$ is the forecast bias at a given lead time [Eq. (2)], and $M(t)$ is the total number of forecasts.

Forecast metrics are computed between matched wave objects in the model and perfect forecast datasets. This ensures that CCKW phasing errors do not inadvertently penalize diagnostics of wave strength or structure. For simplicity and to minimize the impact of outliers, we only include CCKW and EW error statistics for systems that exist in observations at the time of model initialization. This is similar to the criteria implemented by Elless and Torn (2018), which only included EWs that were tracked since the initial conditions. For CCKWs, we further limit error statistics to times when the perfect forecast wave amplitude exceeds 0.75 standard deviations. Our results were insensitive to these choices during testing, though models do appear to struggle more to capture CCKWs that do not exist at initialization (not shown).

3. CCKW forecast metrics

a. General characteristics

We now evaluate CCKW forecast errors in the DIMOSIC and AIFS models. Though CCKWs can be tracked using both precipitation and OLR data, only precipitation data are available across all of the forecast models. As such, while OLR tracks are used in our initial evaluation, we will primary focus on the precipitation-based CCKW statistics.

The cumulative success rates, defined here as a model's ability to capture waves that exist at the time of model initialization, are shown for both the precipitation and OLR tracking methods (Fig. 3). Success rates vary by forecast model and tracking technique but generally range from 75% to 95%.[4] This corresponds to anywhere from 25 to 118 CCKWs that are not captured at all in model forecasts. Forecast models are also more likely to capture stronger CCKWs, as indicated by the orange bars. Some notable intermodel differences exist; namely, the ICON, ICON ReRun, and AIFS models stand out as having relatively higher success rates, while the Met Office, CMC, and Météo-France (Met. France) models have relatively lower success rates (Fig. 3a). The ICON models are more comparable to the IFS models when using OLR tracking, but they still outperform the Met Office and System for High-Resolution Prediction on Earth-to-Local Domains (SHIELD) systems (Fig. 3b).

A summary of RMSE and forecast bias as a function of lead time is shown in Fig. 4. All of the operational models underestimate CCKW strength throughout their lifetimes, though some models (particularly ICON and AIFS) perform noticeably better than others at later lead times (Figs. 4c,f). Also notable is the behavior of the RMSE curves for CCKW strength (Fig. 4c). An initial steep increase in errors appears to flatten out by day 5, even decreasing at extremely long lead times. While this has the resemblance of error saturation (e.g., Boffetta and Musacchio 2017; Judt 2018), it also could be influenced by sample dropout at longer lead times. Meanwhile, the IFS models appear to propagate the CCKW's precipitation envelope the fastest, while SHIELD exhibits markedly slower propagation (Figs. 4a,b,d,e).

One caveat is that the overall sign of the speed and track bias appears to depend on whether precipitation or OLR is used for CCKW tracking. Figure 5 shows the forecast statistics (when available) using OLR-based tracks. While precipitation-based tracking suggests that most models propagate CCKW precipitation too quickly, OLR-based tracking often indicates a more neutral or slow bias for OLR. We hypothesize that a few factors could influence these differences. The underlying observed CCKW samples may differ depending on the tracking

[4] The absolute success rate is much smaller when using model data that do not have observations appended prior to initialization (not shown). This suggests that filtered observations can project onto model time steps, potentially inflating the overall success rates shown in Fig. 3. However, we find similar relative differences between models using this model-only approach, indicating that this conclusion is robust.

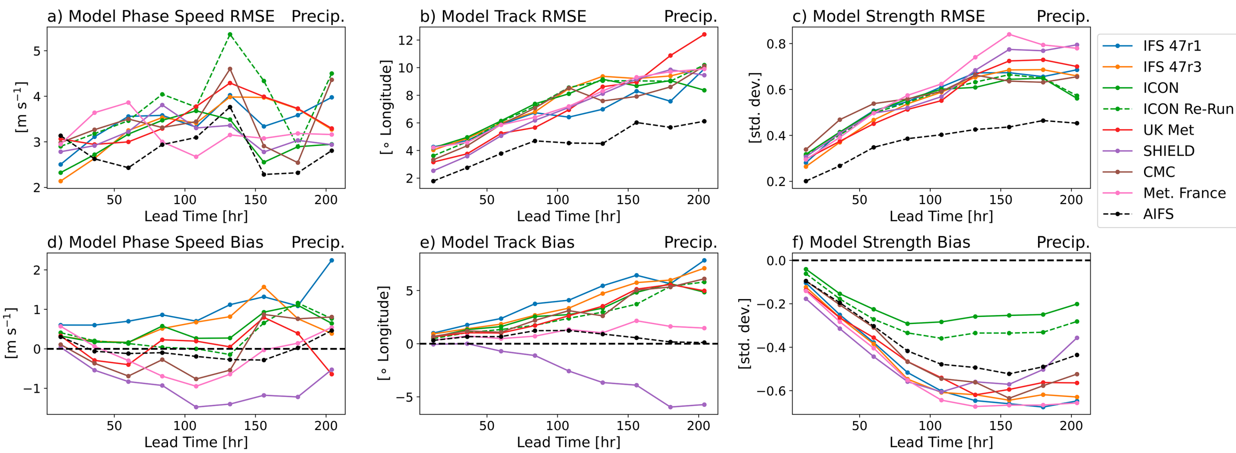

FIG. 4. Summary of CCKW forecast errors as a function of lead time. The bias-corrected RMSE of (a) CCKW phase speed, (b) CCKW track, and (c) CCKW strength, all using the precipitation tracking data. (d)–(f) As in (a)–(c), but for the model bias. We only include CCKWs that exist in observations at the time of model initialization and have a strength of at least 0.75 standard deviations.

method (e.g., Fig. 1a). Additionally, OLR fields are not directly interchangeable with those of precipitation; OLR measures outgoing radiation at the top of clouds, which is often, but not always, associated with rainfall. Despite these differences, errors in phase, track, and strength for individual CCKWs remain correlated across the precipitation- and OLR-based tracks (Fig. S4). Furthermore, relative intermodel differences in propagation and strength are consistent.

A few modeling systems stand out in their ability to capture CCKWs. AIFS consistently outperforms physics-driven models in simulating CCKW propagation and strength, particularly in the short-to-medium range (12–120 h). Its RMSE is substantially lower than that of other systems (dashed black line; Figs. 4a–c), and its propagation bias remains near zero across all lead times (Figs. 4d,e). Both ICON systems also have dramatically reduced strength biases as compared to the other numerical models, as well as relatively reduced RMSEs at longer lead times (120+ h). However, ICON strength RMSEs are more comparable to other models at shorter lead times. Furthermore, intermodel differences are more evident when using precipitation-based tracking than OLR (solid and dashed green lines; Figs. 4c,f and 5c,f). The composite RMSE and biases across all lead times support similar conclusions (full statistics provided in Table S1). Statistical significance testing of each model's CCKW errors across all lead times (95% threshold; not shown) indicates that AIFS, ICON, and ICON ReRun have significantly lower strength RMSEs than those of the other models. AIFS also demonstrates a significantly lower track RMSE than the dynamical models.

b. *Further validation of AIFS*

The DIMOSIC time period analyzed here extends from June 2018 to June 2019, which falls within the training period for the AIFS v1.0 model (Lang et al. 2024b). While the data used to evaluate CCKW strength and location, rainfall from IMERG (Huffman et al. 2023), are not directly used in training AIFS, data used to evaluate the CCKW structure are (ERA5). It is possible that evaluating AIFS during this period

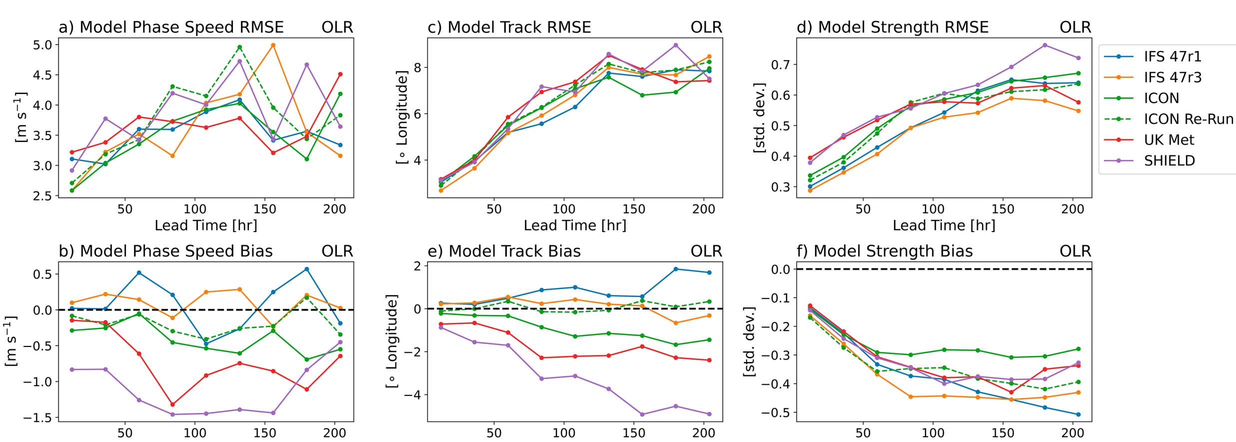

FIG. 5. As in Fig. 4, but using OLR-based wave tracking. Note that OLR output is not available for all forecast models.

TABLE 2. Description of additional AIFS and ECMWF operational models analyzed over time periods differing from the DIMOSIC period.

Abbreviation	Period	Description
AIFS (original)	6 Jun 2018–4 Jun 2019	AIFS during DIMOSIC period
AIFS (2023)	1 Sep 2023–31 Oct 2023	AIFS during 2023 period
AIFS (2024)	1 Apr 2024–1 Sep 2024	AIFS during 2024 period
IFS (2024)	1 Apr 2024–1 Sep 2024	IFS (v48r1) operational model during 2024 period
IFS EC (2024)	1 Apr 2024–1 Sep 2024	IFS ensemble (v48r1) control member during 2024 period

could indirectly inflate this model's apparent forecast skill, complicating interpretation.

To address this limitation, we consider CCKW forecast metrics from AIFS simulation run during time periods outside the model's training window. This includes a month and a half in 2023 and 5 months in 2024 (a longer period of time is utilized in 2024 to foster robust intermodel comparisons). For these new time periods, non-ECMWF models run with identical initial conditions are not available. However, operational ECMWF IFS simulations are available for the 2024 period and are used for comparison. These model runs are summarized in Table 2.

An analysis of basic CCKW forecast statistics reveals several key findings (Fig. 6). Despite some expected variability, the magnitudes of CCKW strength errors (both RMSE and bias) in AIFS are largely consistent across the three time periods. For example, RMSE increases from approximately 0.2–0.3 standard deviations at short lead times to 0.4–0.5 standard deviations at longer lead times (Figs. 6a,d). Although direct comparisons across time periods are challenging, these values remain well below the RMSEs produced by the DIMOSIC dynamical models (e.g., Figs. 4c,f). The relatively tight clustering of AIFS forecast skill, even when the model is run outside its training period, increases our confidence in the model's ability to produce accurate CCKW forecasts.

Furthermore, the additional AIFS runs produced for 2024 clearly outperform the corresponding ECMWF dynamical models (Figs. 6b,c,e,f), with substantially lower CCKW track and strength RMSEs. Wave strength, in particular, is slightly less biased toward weaker values. Similar improvements are observed across other metrics, such as CCKW success rate (not shown). We caution that forecasts from other periods cannot be directly extrapolated to the DIMOSIC period. Nevertheless, these results suggest that AIFS provides consistent and relatively accurate CCKW forecasts even outside its training period.

c. *Errors in CCKW dynamical fields*

We now evaluate whether numerical simulations accurately capture the structure of CCKWs by examining errors in unfiltered environmental fields surrounding tracked waves. These include precipitation, divergence, temperature, and, when available, specific humidity,[5] which all capture the main moist dynamics of CCKWs (Fig. 7).

Errors in wave-centered divergence and precipitation largely complement the results shown in Fig. 4. Simulated CCKWs typically exhibit reduced precipitation, weaker lower-level convergence, and diminished upper-level divergence relative to observations, consistent with the negative CCKW strength bias described previously (Figs. 7d–f). The AIFS and ICON models again demonstrate improved skill in capturing the divergence and precipitation associated with CCKWs, though both remain biased toward weaker magnitudes. Given that precipitation in CCKWs is closely linked to the wave's dynamical and thermodynamical structure, it is unsurprising that the underestimation of CCKW strength corresponds with a weakening of associated wind anomalies.

Supporting this link between precipitation and wave dynamics, we find strong correlations between model errors in CCKW dynamical fields, represented by lower- and upper-level divergence, and those of precipitation and CCKW strength (Fig. 8). Across all models, CCKW strength errors are positively correlated with errors in precipitation and upper-level divergence and negatively correlated with errors in lower-level divergence (matrix rows 3–4). Correlations are even stronger between divergence and precipitation errors (rows 6–7), and upper- and lower-level divergence errors are themselves negatively correlated with one another (row 8). In contrast, errors in the propagation of CCKWs are much less correlated with errors in wave strength and environmental variables (rows 1, 5).

A correspondence between upper- and lower-level divergence errors suggests that our methodology is capturing vertically coherent features of the CCKW structure, rather than artifacts from background noise or unrelated biases. Strong associations between convective and dynamical errors also indicate that a model's ability to fully capture the CCKW's convective envelope is closely linked to its representation of the wave's dynamical structure. These results provide confidence that the models are, to some degree, capturing the convective coupling process itself. This aligns with findings from the modified MPAS-atmosphere (MPAS-A) simulations analyzed by Lawton et al. (2024) and suggests that even imperfect model simulations retain meaningful representations of the convective–dynamical feedbacks central to CCKW evolution.

d. *Interpreting relative model performance*

The spatial, wave-relative structure of model biases can offer valuable insight into why some physics-driven models outperform others. Figure 9 shows the 10°S–10°N wave relative average of environmental biases aggregated across all lead times. The model biases shown in Fig. 7 persist here. Of particular

[5] Specific humidity was only available for IFS 47r1, ICON ReRun, and AIFS.

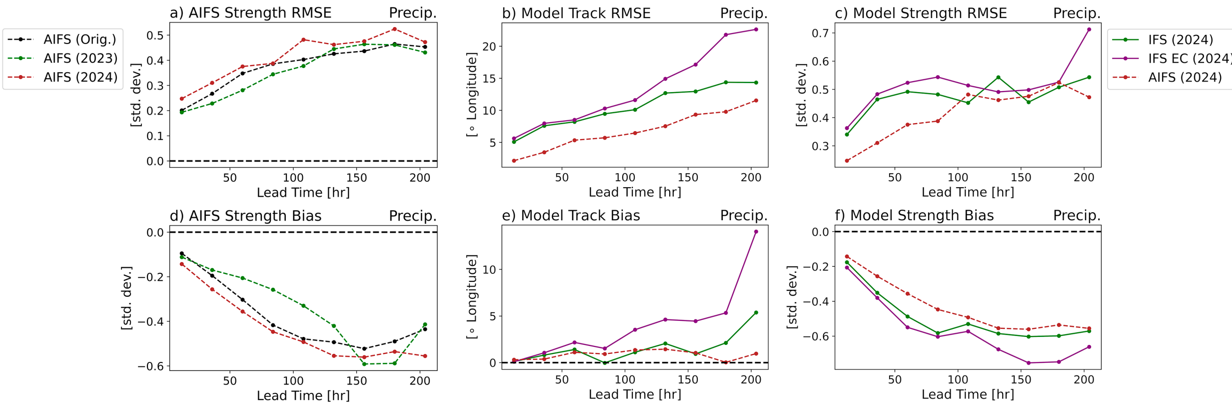

FIG. 6. CCKW forecast errors as a function of lead time for AIFS and ECMWF dynamical models run over additional time periods. (a),(b) As in Figs. 4c and 4f, but comparing AIFS run over three different time periods: the DIMOSIC period, 1.5 months of 2023, and 5 months of 2024. (b),(c),(e),(f) As in Fig. 4, but comparing 2024 forecast statistics for AIFS (dashed lines), the operational IFS (IFS; solid, green lines), and the control member of the IFS ensemble (IFS EC; solid, purple lines).

note is the close alignment between errors in precipitation and those in 850-hPa divergence (Figs. 9a,c). While all forecast models can recreate the dynamical structure of CCKWs in the aggregate (see Fig. S5), deficiencies in CCKW representation extend beyond precipitation to the dynamical fields as well.

These biases likely reflect differences in how models represent thermodynamics and moisture. Figure 9d shows wave-relative 850-hPa temperature biases, revealing 1) persistent mean biases and 2) more positive biases west of the wave center compared to the east. The first component can largely be attributed to each model's tropical mean-state biases (Fig. 10). At and north of the equator, ICON exhibits a pronounced low-level warm bias compared to ERA5 and other models, while CMC and Met. France display strong cold biases (Fig. 10a).

The second component suggests diminished thermodynamic anomalies at and ahead of the wave trough. In CCKWs, a warm anomaly typically leads the CCKW convective maximum at low levels (to the east), followed by a cool anomaly (to the west). Thus, the spatial pattern of 850-hPa temperatures biases is reflective of reduced CCKW-associated thermodynamic anomalies. Additionally, the ICON ReRun model has elevated lower-level specific humidity around CCKWs relative to ERA5 and the IFS model (Fig. S6).

We hypothesize that two mechanisms may contribute to the improved CCKW forecasts in both ICON forecast models. First, mean-state biases in temperature and moisture may affect instability and precipitation ahead of, and within, the CCKW's convective envelope. This could promote increased convective activity, and thus coupling and wave growth, in the ICON forecasts. Supporting this are the high precipitation biases in ICON's tropical mean state, especially compared to models like CMC and Met. France which are cool biased and have relatively reduced precipitation (Fig. 10b). ICON's rainfall overestimation over the tropical oceans has also been documented in previous studies (Magnusson et al. 2022; Jung and Knippertz 2023). Perhaps not coincidentally, the CMC and Met. France models also exhibit more negative CCKW strength biases than that of the ICON models. Second, ICON may more accurately

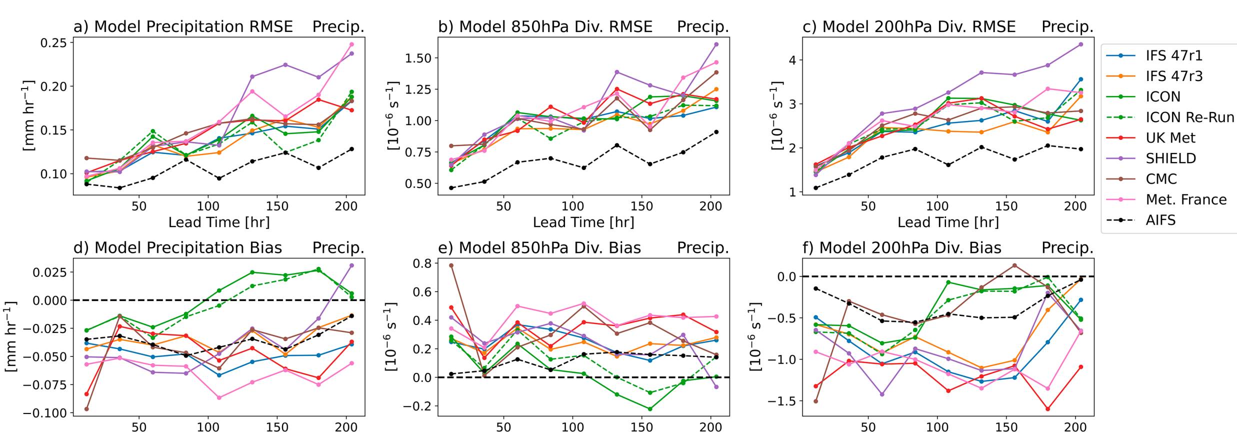

FIG. 7. As in Figs. 4a–f, but for errors in the unfiltered precipitation, 850-hPa divergence, and 200-hPa divergence averaged within 10° longitude of the CCKW's center from 10°S to 10°N.

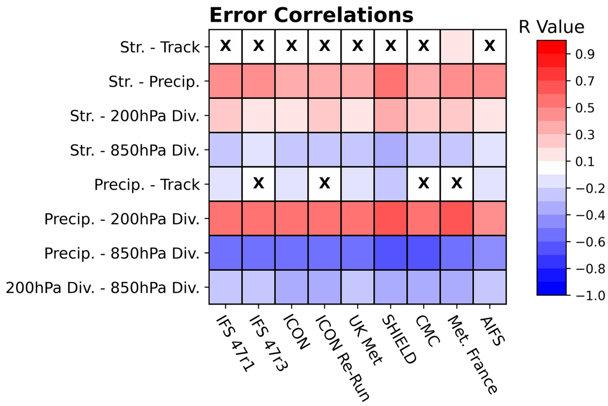

FIG. 8. Graphic showing intramodel correlations between errors in various wave characteristics, computed across each CCKW and model time step. Environmental variables are averaged within 10° longitude of the tracked CCKW center from 10°S to 10°N. In all subpanels, box colors represent Pearson correlation coefficients (R), and correlations not statistically significant at the 95% level are marked with an "X." This analysis is conducted using the precipitation-based CCKW tracks.

simulate the convective coupling and other dynamical processes essential to CCKW growth and propagation, as suggested by the alignment between reduced 850-hPa divergence errors and improved precipitation and wave strength. This aligns with work by Jung and Knippertz (2023) showing that the ICON model tends to produce realistic depictions of tropical waves, including CCKWs, albeit with underestimated intensities. Other model-specific factors, such as their ability to simulate surface feedbacks, could also play a role.

Implicit in these results is that the improved representation of CCKW strength in the two ICON forecast models coincided with sizable mean-state biases. While other models also exhibit mean-state biases, this highlights an important point: Equatorial waves are just one aspect of the tropical atmosphere. Improvements in CCKW forecasts do not necessarily imply better forecasts for other atmospheric fields.

Our findings also highlight the strong performance of the AIFS model in representing CCKW characteristics, including their strength, track, and surrounding temperature anomalies. Because it is a data-driven model, it is unclear that the AIFS result can be attributed to CCKW growth and propagation processes in the same way they can be for physics-driven models. AIFS is trained on ERA5 reanalysis data, so it is not surprising that it better captures the wave's dynamical features as compared to the precipitation envelope, which use IMERG data as a reference (Fig. 9). Nevertheless, these findings demonstrate the AIFS model's capability to accurately simulate CCKWs. Supporting this are results indicating that AIFS also exhibits relatively strong CCKW forecast skill outside its training window (Fig. 6). As a data-driven model, AIFS may not need to explicitly simulate the CCKW's convective-coupling processes and may instead rely on "synoptic memory" to propagate these features—potentially giving it an advantage over physics-driven models in some situations.

4. Connecting CCKW errors to regional and dynamical factors

Results from section 3 show that both the DIMOSIC numerical models and the AIFS system generally underestimate the strength and dynamical structure of CCKWs, especially at longer lead times. Next, we leverage our unique method of individually tracking waves to examine these forecast errors in detail.

a. Errors in CCKW growth

We first seek to understand if there are particular stages in the CCKW's lifetime for which forecast errors are more or

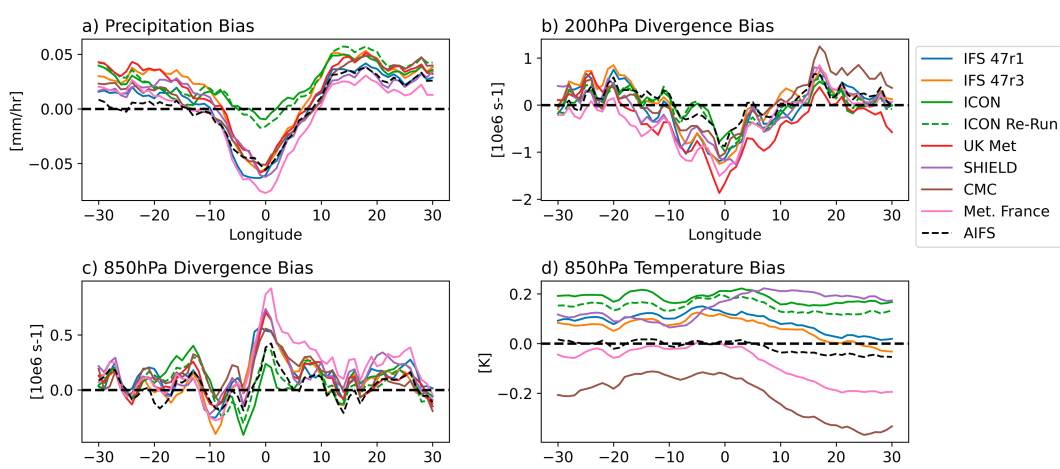

FIG. 9. Graphic showing the spatial distribution of model biases around tracked CCKW centers. Variables are averaged between 10°S and 10°N, and all lead times are included. This includes (a) precipitation error, (b) 200-hPa divergence bias, (c) 850-hPa divergence bias, and (d) 850-hPa temperature bias. Precipitation-based CCKW tracks are used to generate these composites. Note that missing data in the Met Office model's temperature output led us to exclude it from (d).

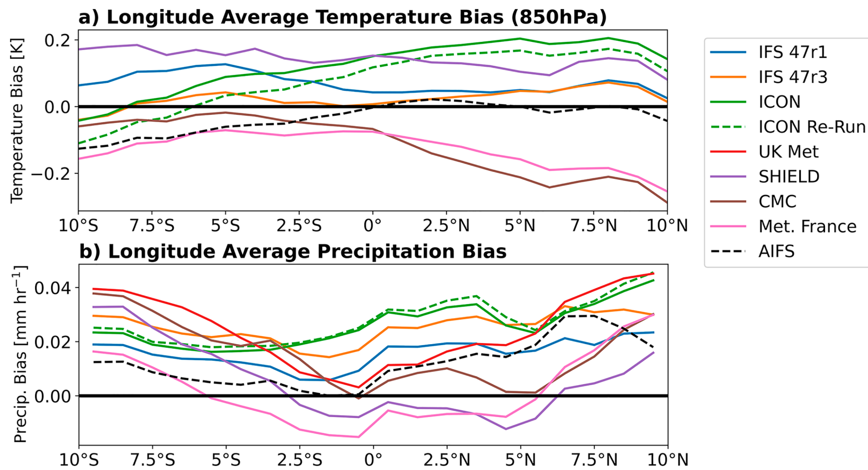

FIG. 10. Diagram showing mean model biases across the DIMOSIC1 period for (a) 850-hPa temperature (K) and (b) precipitation rate (mm h^{-1}), averaged between all longitudes and shown from 10°S to 10°N. Temperature biases use ERA5 as a reference, whereas precipitation biases use IMERG as a reference. As noted in Fig. 9, temperature data were excluded for the Met Office forecast model.

less prominent, which could provide insight into underlying sources of error. Figure 11 shows the RMSE of various metrics, binned by the relative time to the observed wave's peak strength. Times to the left of the vertical dashed line represent forecast errors occurring before the wave reaches its maximum intensity (as defined by filtered rain rate), and times to the right are afterward. This denotation roughly splits the wave's lifetime into its "growth" and "weakening" stages, with errors on the left side of this line primarily corresponding to time periods where the CCKW is expected to be increasing in intensity. For nearly all variables except phase speed, RMSEs decline as the observed wave approaches peak strength and then level off afterward. This result highlights that the largest model errors occur during the wave's intensification phase. Notably, both ICON models' increased performance in representing CCKW strength and precipitation is generally confined to the growth phase. This further suggests that its relative success may stem in part from better representation of processes governing CCKW growth.

While this pattern is consistent across all physics-driven forecast systems, it is notably less prominent in AIFS. The peak-relative drop in CCKW strength RMSE is still present in AIFS, but less pronounced (Fig. 11c). Furthermore, RMSEs for CCKW track and divergence show little or no dependence on the relative time to the wave peak's strength (Figs. 11b,e,f), suggesting that these errors are less tied to the growth or weakening phases. This may highlight a potential advantage of data-driven models. Unlike physics-driven systems, which must accurately represent both convection and their coupling

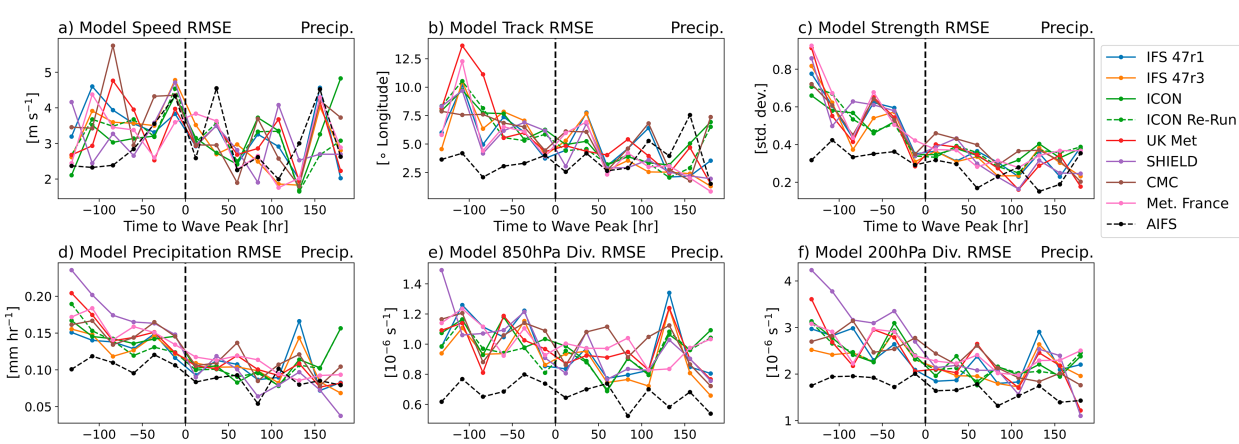

FIG. 11. Summary of model RMSEs binned by the relative time to the reference CCKW's maximum strength, as defined by filtered rain rate. Included RMSE metrics are (a) CCKW phase speed, (b) CCKW longitude, and (c) CCKW strength. RMSEs are for unfiltered environmental variables averaged between 10°S and 10°N and within 10° longitude of the CCKW center, including (d) precipitation, (e) 850-hPa divergence, and (f) 200-hPa divergence.

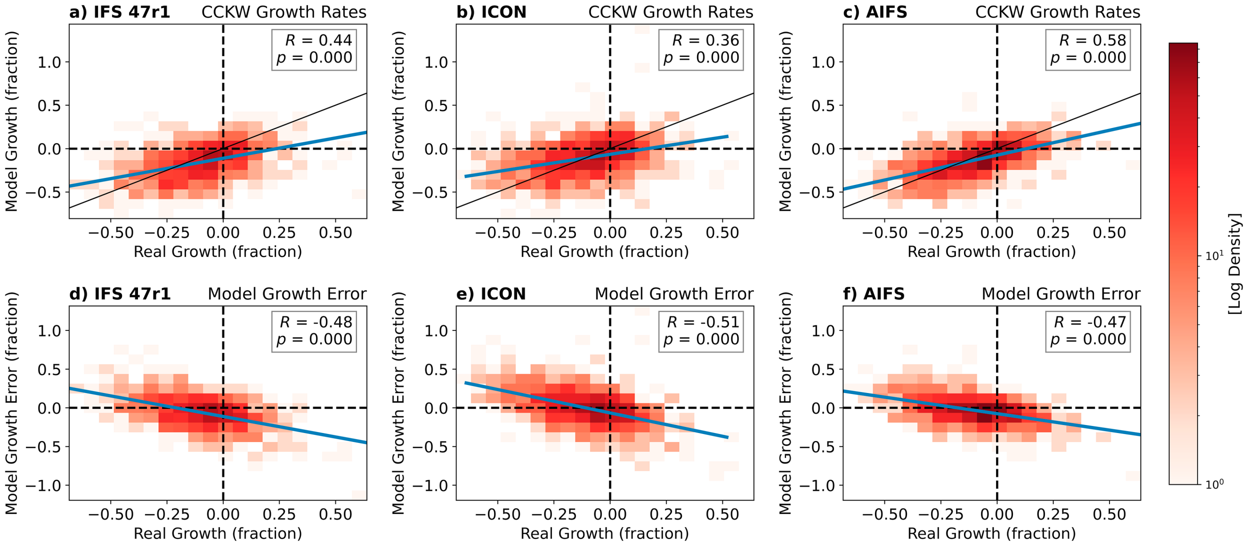

FIG. 12. The analysis of CCKW growth rates and their relationship to other CCKW errors. Two-dimensional histogram showing relationship between the observed (perfect forecast) CCKW growth rates (x axis) and the simulated growth rates (y axis) for (a) IFS 47r1, (b) ICON, and (c) AIFS. Samples are binned and plotted on a logarithmic scale. The linear fit line (blue), $y = x$ line (black), and relevant Pearson's R and p values (bottom right box) are shown for reference. (d)–(f) As in (a)–(c), but with the error in CCKW growth rate plotted on the y axis.

to wave growth to capture CCKWs, AIFS may be better able to emulate observed patterns directly.

Models also struggle with representing CCKW intensity changes, in particular growth. The top rows of panels in Figs. 12a–f illustrate the relationship between errors in CCKW growth rate and observed growth rate in three representative models (results are consistent across the DIMOSIC suite). Models tend to underestimate both CCKW growth and weakening. Nevertheless, a persistent negative bias in CCKW strength, precipitation, and 200-hPa divergence remains even during the weakening phases (not shown), indicating a systematic underrepresentation of wave intensity. We hypothesize that the underestimation of wave growth is related to deficiencies in representing convective coupling. Similarly, errors in CCKW weakening likely stem from a model's initial failure to accurately capture wave growth and peak intensity; if the peak is underestimated, subsequent weakening is also reduced in magnitude.

In addition to these metrics, we also analyzed forecast skill as a function of location (not shown). While some differences exist, we found no evidence of a widespread regional dependence.

b. *Vertical coherence and initial model shock*

We can also verify our wave-following errors more generally using global benchmarks. Figure 13 illustrates the average coherence-squared values between Kelvin-filtered precipitation and divergence. This metric was previously used by Gehne et al. (2022) to identify if a variable has significant correlation with Kelvin-filtered rainfall and to quantify its phase and lead–lag relationships. As demonstrated in Fig. 13a for IMERG and ERA5 divergence data, coherence-squared values are the highest at lower levels (900–800 hPa), with a secondary maximum in the upper levels (200 hPa). Convergence at lower levels leads precipitation, whereas divergence at upper levels lags precipitation. This diagnostic illustrates the in-up-out circulation of CCKWs and their convective coupling. We expect numerical models that accurately represent CCKWs processes exhibit a similar coherence-squared and lead–lag relationship.[6]

Intermodel comparisons of vertical coherence align with our object-based forecast statistics. Figures 13b–d show the coherence-squared and lead–lag relationships at early, middle, and later lead times, respectively. All of the models at least partially capture the lower- and upper-level coherence-squared maxima of observations, as well as the lead–lag precipitation/divergence relationship. However, the ICON model simulations show the strongest coherence at low levels of all of the physics-driven models, closely resembling the vertical pattern seen for observations in Fig. 13a. In contrast, the vertical coherence-squared profiles are less accurate for the SHIELD, Met. France, Met Office, and CMC models. These relative model differences align with the object-oriented forecast errors and demonstrate a connection to each model's ability to realistically couple wave dynamics with precipitation. Furthermore, the profile of vertical coherence for the AIFS model is much larger than the physics-driven models, indicating that the data-driven system is able to recreate the relationship between CCKW precipitation and its dynamics.

[6] We do not expect the magnitude of coherence squared to be comparable for the IMERG/ERA5 reference numerical models, only the vertical structure. Differences between the IMERG and ERA5 datasets means they will inherently be less coherent with one another than a model's divergence with its own precipitation. Indeed, Gehne et al. (2022) found ERA5 precipitation to be much more coherent with ERA5 fields than when using IMERG precipitation.

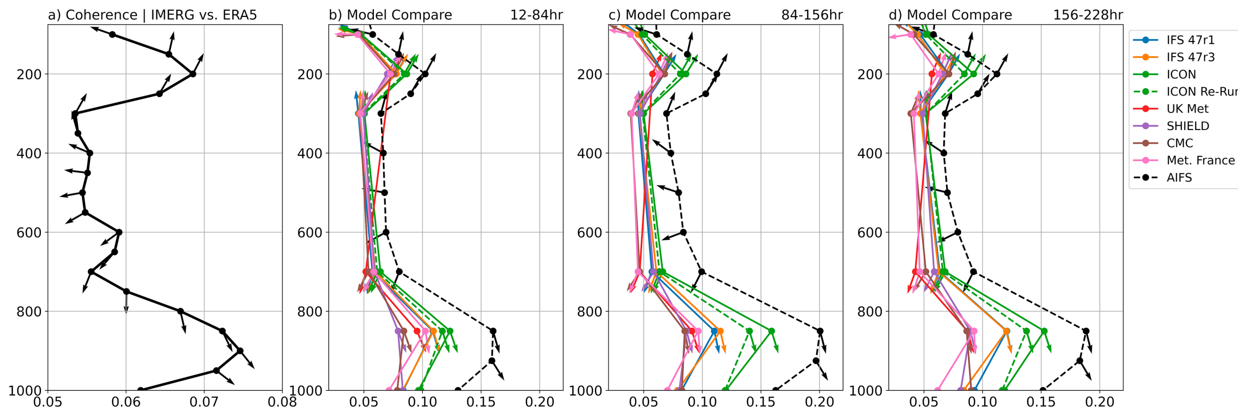

FIG. 13. Diagrams detailing the vertical coherence Kelvin-filtered precipitation and divergence. Coherence is calculated using the diagnostics toolbox developed by Gehne et al. (2022). (a) The average coherence squared for ERA5 divergence with Kelvin-filtered IMERG rainfall. Lines illustrate each model's coherence squared between divergence and Kelvin-filtered rainfall at forecast hours (b) 12–84, (c) 84–156, and (d) 156–228. All cross-spectra values are computed between 10°S and 10°N. Arrows drawn on the figure represent the lagged precipitation–divergence relationship, with upward arrows denoting an in-phase relationship, downward arrows denoting an out-of-phase relationship, rightward arrows indicating precipitation leads divergence, and leftward arrows indicating divergence leads precipitation. Note that different vertical levels are available for each individual numerical model.

Many of the physics-driven models (ICON, ICON ReRun, IFS 47r1/47r3) exhibit a notable increase in lower-level coherence squared between the 12–84- and 84–156-h lead times. This pattern may be linked to the presence of initial model shock. As described by Magnusson et al. (2022), initializing the diverse DIMOSIC model suite using a different analysis field than produced by that model (in this case, from the IFS) can lead to an initial adjustment period. This period is characterized by suppressed precipitation, typically within the first 3 days. The severity of this shock varies by the model: It is especially pronounced in the CMC and Met Office simulations but relatively mild in the IFS and ICON runs (Magnusson et al. 2022, their Fig. 1). The delayed emergence of CCKW convective coupling may, therefore, reflect the time it takes for models to recover from this initial imbalance. Some evidence of this impacting CCKW-relative fields is seen in Fig. 7d, where CCKW-following precipitation in the CMC and Met Office models is exceptionally low biased at the first lead time step, followed by an immediate recovery 24 h later.

This early adjustment period may also help explain some of the intermodel differences in CCKW forecast skill. If a model cannot fully resolve convective coupling during the early forecast hours, it may struggle to accurately capture initial CCKW growth. Both the ICON and the IFS models, all of which were found by Magnusson et al. (2022) to exhibit relatively mild initial shock, generally outperform other simulations in forecasting CCKW structure and evolution. Nevertheless, the extent to which this adjustment influences CCKWs relative to other factors remains unclear.

5. Relationship with easterly waves and interactions

Recent research has shown that interactions between CCKWs and EWs can promote tropical cyclogenesis and localized extreme rainfall events (Ferrett et al. 2020; Latos et al. 2021; Peyrillé et al. 2023; Lawton and Majumdar 2023). This suggests that model deficiencies in either wave type could lead to missed high-impact events. Because previous studies have not quantified how well operational forecast models capture these CCKW–EW interactions, we next evaluate model performance for these events.

a. *Overview of EW forecast skill*

For context, we briefly discuss the forecast skill of tracked EWs in the DIMOSIC models and AIFS. While some previous work has investigated EW forecasts in specific modeling systems (Torn 2010; Elless and Torn 2018), we are not aware of a study that has looked at these forecasts in a large suite of models like DIMOSIC.

The RMSE and bias in EW longitude, latitude, and midtropospheric wave strength—defined as the average 700-hPa curvature vorticity within 600 km of the wave center—are shown in Fig. 14. Forecast skill is evaluated separately for the Atlantic (Figs. 14a–f) and the eastern Pacific (Figs. 14g–l) due to differences in wave characteristics between these basins. RMSEs increase steadily as a function of lead time for all evaluated metrics. Across both basins, models tend to propagate EWs too quickly during the first five simulation days, as indicated by a negative (westward) longitude bias (Figs. 14d,j). This pattern is especially pronounced in the eastern Pacific. This pattern shifts for Atlantic EW longer lead times (5+ days), with most models switching to propagating these waves too slowly. As with longitude, latitude biases also differ by region, particularly at longer lead times.

EW strength biases are especially dependent on forecast lead time. Most models underestimate EW strength at early lead times (0–72 h). In the Pacific, this negative bias tends to persist throughout the forecast. In the Atlantic, however, strength RMSEs and biases vary considerably across models at longer lead times. Regional differences in the role of moisture in EW

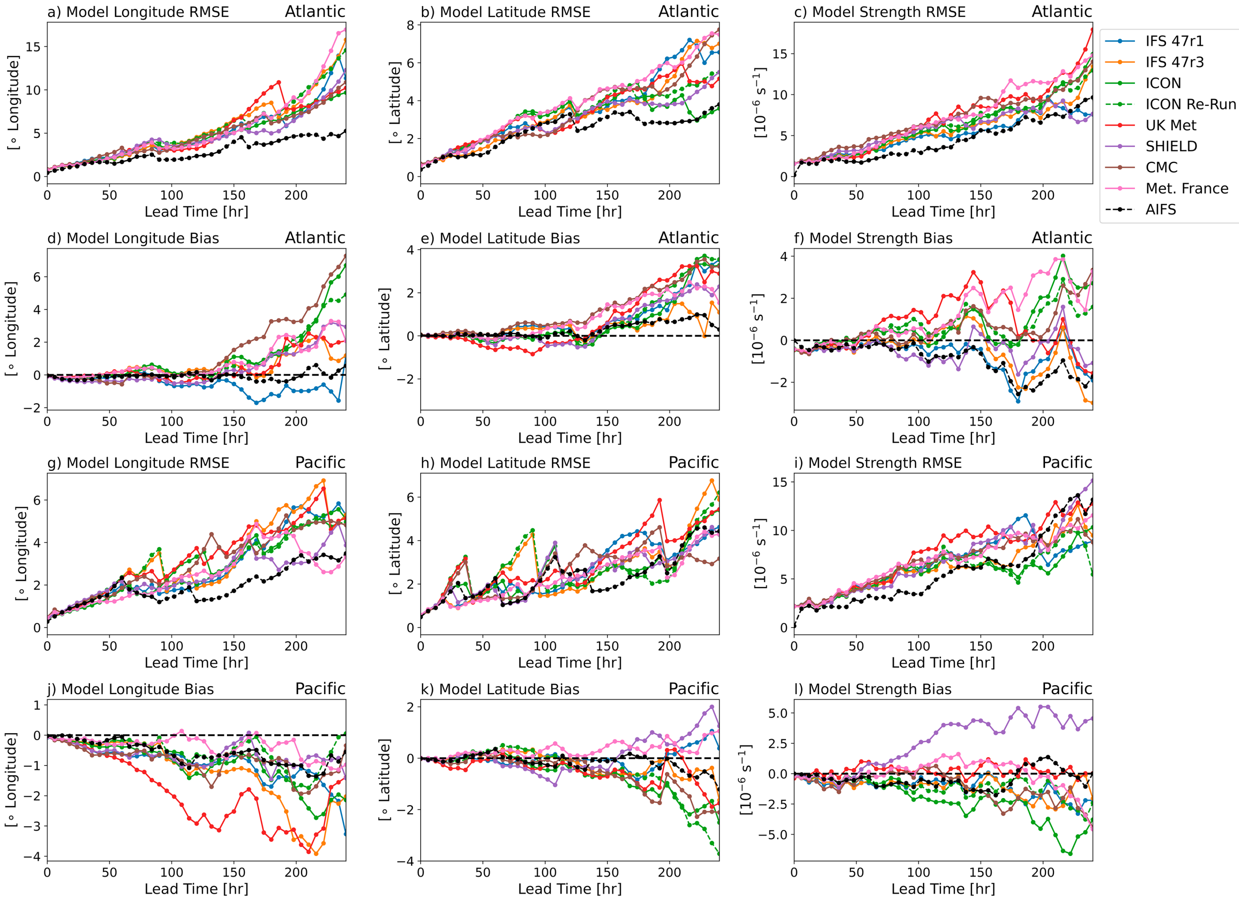

FIG. 14. Summary of EW forecast skill. RMSE for (a) EW longitude, (b) EW latitude, and (c) EW strength in the Atlantic basin as a function of lead time. EW strength is defined as the average 700-hPa curvature vorticity within 600 km of the tracked center. (d)–(f) As in (a)–(c), but for forecast bias. (g)–(l) As in (a)–(f), but in the eastern Pacific. Only EWs from June to October 2018 are included due to limitations in the reference dataset (Lawton et al. 2025).

dynamics, particularly between Atlantic/African and Pacific environments, may be a contributing factor (Vargas Martes et al. 2023). However, establishing the role of these and other factors in influencing wave forecasts will require future work that directly evaluates simulated EW dynamics.

The AIFS model again stands out from the physics-driven models with strikingly reduced RMSE errors and biases for EWs, especially over the Atlantic. Not only are RMSEs in wave track markedly smaller in AIFS than the other models, but forecast bias remains relatively neutral even out to longer lead times (Figs. 14a,b,d,e). As was done for CCKWs (see section 3b), we conducted a separate evaluation of EW forecast skill for 2024, a time period outside the AIFS training period (not shown). This analysis also showed improved Atlantic EW performance in AIFS relative to the ECMWF dynamical models, although skill differences over the eastern Pacific are more comparable.

b. Forecasts of CCKW–EW interactions

Next, we discuss how model inaccuracies in CCKW and EW forecasts may affect the representation of wave superposition. Figure 15 shows the frequency of CCKW–EW interactions from June to October 2018 across the eastern Pacific, Atlantic, and African regions, along with the ability of the DIMOSIC and AIFS models to capture them. A total of 17 events occurred during this period, primarily in the eastern Pacific. Operational models captured less than 50% of these events (Fig. 15b), though performance improves when both waves are present in observations at model initialization (orange bars). Forecast models with better overall CCKW representation (as detailed in section 3), such as IFS and ICON, show slightly higher success rates (e.g., 0.5–0.55 for IFS r7r1 and ICON vs around 0.4 for SHIELD and CMC). Unlike for other metrics, AIFS does not consistently outperform the physics-based models in this context.

Missed interactions are driven both by CCKW and EW forecast deficiencies. This conclusion is illustrated by the "dropout" metric in Fig. 15c, which illustrate whether a missed CCKW–EW interaction was due to a missing CCKW, EW, or both. Even when interactions are captured, they often occur east of their observed location and with weaker CCKW strength than in reality (compared to the perfect forecast; Figs. 15d,e).

Two caveats of Fig. 15 are the limited sample size [due to the regional and temporal coverage of the Lawton et al. (2025) dataset] and the differences in CCKW and EW tracking methodologies.

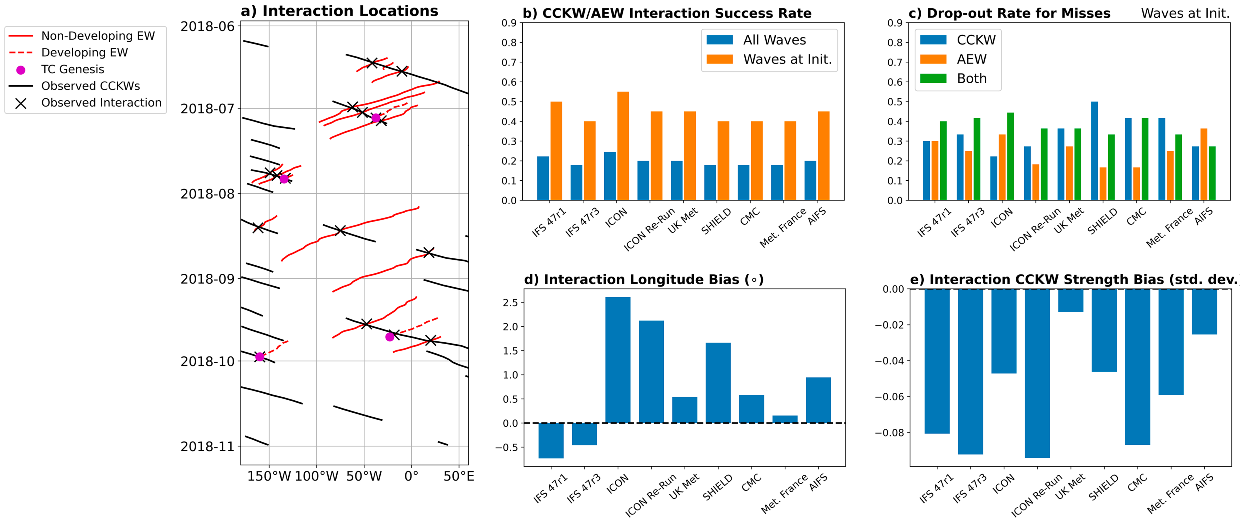

FIG. 15. Figure quantifying CCKW–EW interaction forecast skill in the forecast models. Interactions are identified as when CCKW and EW tracks pass one another in longitude, and numerical models are only evaluated against CCKW–EW passages identified in the reference perfect forecast dataset. (a) The CCKW–EW interactions that occurred in observations (using precipitation-tracked CCKWs) in the June–October 2018 period (black X symbols), with corresponding EW (red) and CCKW (black) tracks overlain. EWs that underwent TC genesis are denoted. We show the (b) success rate of each model in capturing these interactions and (c) the source of "missed" interactions when both waves are present in observations at initialization. We also show each model's average bias in simulating the, (d) longitude and (e) strength of CCKWs at the time of the interaction.

To further validate these results, we also computed statistics for CCKW–EW interactions using EW tracks generated similarly to those of CCKWs but from precipitation filtered using the TD band (see section 2d; Fig. S7). The general conclusions from Fig. 15 also hold here: Forecast models miss over 50% of wave interactions due to deficiencies in both CCKW and EW representation, and those events that are captured occur eastward and with weaker CCKWs than in reality. Overall, these results highlight that operational models often struggle to simulate the superposition of CCKWs and EWs, in part due to deficiencies in wave representation.

6. Conclusions

a. *Summary and discussion*

In this paper, we developed an object-oriented framework to evaluate forecasts of CCKWs and EWs across a suite of operational forecast models. These forecasts originated from the DIMOSIC project (Magnusson et al. 2022), which we supplemented with additional models, including ECMWF's newly operational data-driven AIFS (Lang et al. 2024a,b). Compared to previous work, this framework enables more detailed quantification of forecast performance as a function of wave characteristics, life cycle phase, and environmental context.

We show that all of the analyzed numerical models underestimate the strength of CCKWs, as indicated by errors in wave amplitude, precipitation, and divergence profiles. In contrast, forecasts of CCKW phase speed and position showed greater variability, depending on both the model and the wave tracking method used. Nevertheless, some forecast models, like IFS (47r1 and 47r3) and ICON, consistently propagate CCKW precipitation and OLR faster than others.

Numerical models particularly struggle to capture wave growth processes. For example, CCKW forecast errors are especially large during the wave's growth phase. Supporting this conclusion, better-performing models exhibited reduced low-level divergence errors and greater coherence between their vertical divergence profiles and filtered rainfall compared to the other models. These results support the idea that CCKW forecast errors are driven in part by deficiencies in how models represent convective coupling and its associated processes. This hypothesis has been raised in previous studies showing that CCKW representation is sensitive to the choice of cumulus parameterization and tends to improve with more explicitly resolved convection (e.g., Dias et al. 2018; Bengtsson et al. 2019; Gehne et al. 2022; Lee et al. 2025). However, prior work has typically focused on a small number of models or case studies, often lacking a consistent framework to evaluate wave life cycle or structural evolution. In contrast, our study systematically evaluates a large set of modeling systems using a unified object-based tracking approach.

It is not clear, however, if improvements in CCKW forecasts are reflective of improvements in a model's overall forecast performance. This is exemplified by the performance of the ICON simulations. Although the ICON models generally outperform the other physics-based models in representing CCKW strength, their forecasts exhibit substantial warm biases in low-level temperature, as well as widespread positive biases in tropical-mean rainfall. In contrast, several models with relatively poor CCKW representation display mean-state biases of the opposite sign. This suggests that mean-state errors can influence CCKW forecasts and highlights that improved CCKW skill does not necessarily imply greater overall forecast accuracy nor does it guarantee that the forecasts are improved for physically consistent reasons.

We also evaluated the ability of these models to capture CCKW–EW interactions. We find that numerical models captured less than 50% of observed CCKW–EW interaction events. The failure to capture CCKW–EW interactions was attributable to deficiencies in both CCKW and EW representation. Even when interactions were captured, they generally occurred east of their observed location and with reduced CCKW intensity. We speculate that these errors could have important consequences on forecasts of extreme weather, as previous studies have shown that such interactions can enhance the likelihood of tropical cyclone genesis and increase the probability of localized extreme precipitation (Ferrett et al. 2020; Latos et al. 2021; Peyrillé et al. 2023; Lawton and Majumdar 2023).

Finally, the AIFS system showed remarkable skill in representing both CCKWs and EWs. The primary analysis period was included in the AIFS training dataset, which may have inflated forecast skill. However, additional analysis of AIFS forecasts outside the training window demonstrates that enhanced wave forecast skill is largely maintained, providing increased confidence in our results. Overall, these results illustrate that data-driven models like AIFS may play an important role in advancing tropical weather forecasting.

b. *Implications and future work*

These results demonstrate the large gap that remains in our ability to accurately forecast CCKWs on medium-range time scales. Our work builds on prior studies showing that forecast models often struggle with CCKW representation, which may limit the broader utility of these waves in improving tropical predictability (e.g., Dias et al. 2018; Schreck et al. 2020; Yang et al. 2021; Dias et al. 2023). The widespread underrepresentation of CCKW strength suggests that forecasts of these waves and their interactions should be interpreted with caution, especially when used in the context of rainfall and TC genesis prediction.

Our findings motivate further investigation into the physical drivers of forecast successes and failures and whether or not certain environmental regimes provide windows of opportunity for increased predictability. Future modeling studies designed to probe how internal processes contribute to error growth could help test these ideas and inform future model development. Furthermore, as this study did not quantify the direct link between forecast deficiencies and the prediction of extreme events, subsequent research should examine how these errors translate into tangible impacts. One limitation of the DIMOSIC dataset used here is the relatively coarse set of available vertical levels and variables, highlighting a need for follow-up work more directly focused on the vertical structure of tropical waves.

Finally, this work underscores the promise of data-driven systems like AIFS. Future work should test additional data-driven models to evaluate whether they can maintain skill in regimes where physics-based models currently fall short.

Acknowledgments. We thank Maria Gehne and Juliana Dias for discussions that greatly improved this work. We also appreciate helpful feedback from NSF NCAR internal reviewer George Bryan and three anonymous external reviewers. We thank the participating groups of DIMOSIC for their efforts in developing the model data used in this study. This material is based upon work supported by the NSF National Center for Atmospheric Research, which is a major facility sponsored by the U.S. National Science Foundation under Cooperative Agreement 1852977. We acknowledge computing support from the Casper system (https://ncar.pub/casper).

Data availability statement. The DIMOSIC model data are available upon request by contacting author Magnusson. Code and weights to run AIFS v1.0 can be found on Hugging Face (https://huggingface.co/ecmwf/aifs-single-1.0). ERA5 data were obtained via the Copernicus Climate Data Store at https://cds.climate.copernicus.eu. IMERG data were obtained via the NSF NCAR Research Data Archive and GES DISC (Huffman et al. 2023). OLR data were obtained from NOAA National Centers for Environmental Information (Lee and NOAA CDR Program 2014). Python code for CCKW tracking and select forecast metrics are available publicly in a GitHub repository (https://github.com/qlawton/cckw_tracking). The reference and model wave tracks used in this study, along with calculated forecast errors, are also available in an online repository (https://doi.org/10.5281/zenodo.15660583). EW tracks were generated via the QTrack python module v0.0.4, first developed by Lawton et al. (2022) and updated by Lawton et al. (2025). The QTrack module is available on GitHub (https://github.com/qlawton/QTrack), and historical tracks are available in an online repository (https://doi.org/10.5281/zenodo.13350859).

REFERENCES

Adames, A. F., D. Kim, S. K. Clark, Y. Ming, and K. Inoue, 2019: Scale analysis of moist thermodynamics in a simple model and the relationship between moisture modes and gravity waves. *J. Atmos. Sci.*, **76**, 3863–3881, https://doi.org/10.1175/JAS-D-19-0121.1.

Bain, C. L., K. D. Williams, S. F. Milton, and J. T. Heming, 2014: Objective tracking of African easterly waves in Met Office models. *Quart. J. Roy. Meteor. Soc.*, **140**, 47–57, https://doi.org/10.1002/qj.2110.

Bengtsson, L., and Coauthors, 2019: Convectively coupled equatorial wave simulations using the ECMWF IFS and the NOAA GFS cumulus convection schemes in the NOAA GFS model. *Mon. Wea. Rev.*, **147**, 4005–4025, https://doi.org/10.1175/MWR-D-19-0195.1.

Boffetta, G., and S. Musacchio, 2017: Chaos and predictability of homogeneous-isotropic turbulence. *Phys. Rev. Lett.*, **119**, 054102, https://doi.org/10.1103/PhysRevLett.119.054102.

Brammer, A., and C. D. Thorncroft, 2015: Variability and evolution of African easterly wave structures and their relationship with tropical cyclogenesis over the eastern Atlantic. *Mon. Wea. Rev.*, **143**, 4975–4995, https://doi.org/10.1175/MWR-D-15-0106.1.

Burpee, R. W., 1972: The origin and structure of easterly waves in the lower troposphere of North Africa. *J. Atmos. Sci.*, **29**, 77–90, https://doi.org/10.1175/1520-0469(1972)029<0077:TOASOE>2.0.CO;2.

Cruz, J. B., J. M. Castanheira, and C. C. DaCamara, 2024: Local identification of equatorial Kelvin waves in real-time operational forecasts. *Quart. J. Roy. Meteor. Soc.*, **150**, 2440–2457, https://doi.org/10.1002/qj.4717.

Dias, J., and O. Pauluis, 2011: Modulations of the phase speed of convectively coupled Kelvin waves by the ITCZ. *J. Atmos. Sci.*, **68**, 1446–1459, https://doi.org/10.1175/2011JAS3630.1.

——, M. Gehne, G. N. Kiladis, N. Sakaeda, P. Bechtold, and T. Haiden, 2018: Equatorial waves and the skill of NCEP and ECMWF numerical weather prediction systems. *Mon. Wea. Rev.*, **146**, 1763–1784, https://doi.org/10.1175/MWR-D-17-0362.1.

——, ——, ——, and L. Magnusson, 2023: The role of convectively coupled equatorial waves in sub-seasonal predictions. *Geophys. Res. Lett.*, **50**, e2023GL106198, https://doi.org/10.1029/2023GL106198.

Dominguez, C., J. M. Done, and C. L. Bruyère, 2020: Easterly wave contributions to seasonal rainfall over the tropical Americas in observations and a regional climate model. *Climate Dyn.*, **54**, 191–209, https://doi.org/10.1007/s00382-019-04996-7.

Elless, T. J., and R. D. Torn, 2018: African easterly wave forecast verification and its relation to convective errors within the ECMWF ensemble prediction system. *Wea. Forecasting*, **33**, 461–477, https://doi.org/10.1175/WAF-D-17-0130.1.

Engel, T., A. H. Fink, P. Knippertz, G. Pante, and J. Bliefernicht, 2017: Extreme precipitation in the West African cities of Dakar and Ouagadougou: Atmospheric dynamics and implications for flood risk assessments. *J. Hydrometeor.*, **18**, 2937–2957, https://doi.org/10.1175/JHM-D-16-0218.1.

Ferrett, S., G.-Y. Yang, S. J. Woolnough, J. Methven, K. Hodges, and C. E. Holloway, 2020: Linking extreme precipitation in Southeast Asia to equatorial waves. *Quart. J. Roy. Meteor. Soc.*, **146**, 665–684, https://doi.org/10.1002/qj.3699.

Gehne, M., B. Wolding, J. Dias, and G. N. Kiladis, 2022: Diagnostics of tropical variability for numerical weather forecasts. *Wea. Forecasting*, **37**, 1661–1680, https://doi.org/10.1175/WAF-D-21-0204.1.

Herman, M. J., Z. Fuchs, D. J. Raymond, and P. Bechtold, 2016: Convectively coupled Kelvin waves: From linear theory to global models. *J. Atmos. Sci.*, **73**, 407–428, https://doi.org/10.1175/JAS-D-15-0153.1.

Hersbach, H., and Coauthors, 2020: The ERA5 global reanalysis. *Quart. J. Roy. Meteor. Soc.*, **146**, 1999–2049, https://doi.org/10.1002/qj.3803.

Hollis, M. A., R. R. McCrary, J. P. Stachnik, C. Lewis-Merritt, and E. R. Martin, 2024: A global climatology of tropical easterly waves. *Climate Dyn.*, **62**, 2317–2332, https://doi.org/10.1007/s00382-023-07025-w.

Hopsch, S. B., C. D. Thorncroft, and K. R. Tyle, 2010: Analysis of African easterly wave structures and their role in influencing tropical cyclogenesis. *Mon. Wea. Rev.*, **138**, 1399–1419, https://doi.org/10.1175/2009MWR2760.1.

Huaman, L., E. D. Maloney, C. Schumacher, and G. N. Kiladis, 2021: Easterly waves in the east Pacific during the OTREC 2019 field campaign. *J. Atmos. Sci.*, **78**, 4071–4088, https://doi.org/10.1175/JAS-D-21-0128.1.

Huffman, G. J., D. T. Bolvin, E. J. Nelkin, and J. Tan, 2023: GPM IMERG final precipitation l3 1 day 0.1 degree x 0.1 degree v07. Goddard Earth Sciences Data and Information Services Center (GES DISC), accessed 15 September 2024, https://doi.org/10.5067/GPM/IMERGDF/DAY/07.

Janiga, M. A., C. J. Schreck, J. A. Ridout, M. Flatau, N. P. Barton, E. J. Metzger, and C. A. Reynolds, 2018: Subseasonal forecasts of convectively coupled equatorial waves and the MJO: Activity and predictive skill. *Mon. Wea. Rev.*, **146**, 2337–2360, https://doi.org/10.1175/MWR-D-17-0261.1.

Judt, F., 2018: Insights into atmospheric predictability through global convection-permitting model simulations. *J. Atmos. Sci.*, **75**, 1477–1497, https://doi.org/10.1175/JAS-D-17-0343.1.

——, and R. Rios-Berrios, 2021: Resolved convection improves the representation of equatorial waves and tropical rainfall variability in a global nonhydrostatic model. *Geophys. Res. Lett.*, **48**, e2021GL093265, https://doi.org/10.1029/2021GL093265.

Jung, H., and P. Knippertz, 2023: Link between the time-space behavior of rainfall and 3D dynamical structures of equatorial waves in global convection-permitting simulations. *Geophys. Res. Lett.*, **50**, e2022GL100973, https://doi.org/10.1029/2022GL100973.

Kiladis, G. N., M. C. Wheeler, P. T. Haertel, K. H. Straub, and P. E. Roundy, 2009: Convectively coupled equatorial waves. *Rev. Geophys.*, **47**, RG2003, https://doi.org/10.1029/2008RG000266.

Knippertz, P., and Coauthors, 2022: The intricacies of identifying equatorial waves. *Quart. J. Roy. Meteor. Soc.*, **148**, 2814–2852, https://doi.org/10.1002/qj.4338.

Lam, R., and Coauthors, 2023: Learning skillful medium-range global weather forecasting. *Science*, **382**, 1416–1421, https://doi.org/10.1126/science.adi2336.

Lang, S., and Coauthors, 2024a: AIFS—ECMWF'S data-driven forecasting system. arXiv, 2406.01465v2, https://doi.org/10.48550/ARXIV.2406.01465.

——, and Coauthors, 2024b:First update to the AIFS. ECMWF, https://doi.org/10.21957/DF5DEA5B13.

Latos, B., and Coauthors, 2021: Equatorial waves triggering extreme rainfall and floods in southwest Sulawesi, Indonesia. *Mon. Wea. Rev.*, **149**, 1381–1401, https://doi.org/10.1175/MWR-D-20-0262.1.

Lawton, Q. A., and S. J. Majumdar, 2023: Convectively coupled Kelvin waves and tropical cyclogenesis: Connections through convection and moisture. *Mon. Wea. Rev.*, **151**, 1647–1666, https://doi.org/10.1175/MWR-D-23-0005.1.

——, ——, K. Dotterer, C. Thorncroft, and C. J. Schreck III, 2022: The influence of convectively coupled Kelvin waves on African Easterly Waves in a wave-following framework. *Mon. Wea. Rev.*, **150**, 2055–2072, https://doi.org/10.1175/MWR-D-21-0321.1.

——, R. Rios-Berrios, S. J. Majumdar, R. Emerton, and L. Magnusson, 2024: The representation of convectively coupled Kelvin waves in simulations with modified wave amplitudes. *J. Adv. Model. Earth Syst.*, **16**, e2023MS004187, https://doi.org/10.1029/2023MS004187.

——, B. Weiser, and S. J. Majumdar, 2025: On the interannual variability of African easterly waves and its relationship with the El Niño–Southern Oscillation. *J. Climate*, **38**, 5791–5808, https://doi.org/10.1175/JCLI-D-25-0113.1.

Lee, H.-T., and NOAA CDR Program, 2014: NOAA Climate Data Record (CDR) of daily Outgoing Longwave Radiation (OLR), version 1.2. NOAA National Centers for Environmental Information, accessed 5 October 2024, https://doi.org/10.7289/V5SJ1HH2.

Lee, S.-H., S.-H. Park, M.-T. Chien, and D. Kim, 2025: Simulations of convectively coupled Kelvin waves (CCKWs) with three different cumulus parameterization schemes. *J. Geophys. Res. Atmos.*, **130**, e2024JD042738, https://doi.org/10.1029/2024JD042738.

Liebman, B., and C. Smith, 1996: Description of complete (interpolated) outgoing longwave radiation dataset. *Bull. Amer. Meteor. Soc.*, **77**, 1275–1277, https://doi.org/10.1175/1520-0477-77.6.1274.

Lubis, S. W., and C. Jacobi, 2015: The modulating influence of convectively coupled equatorial waves (CCEWs) on the variability of tropical precipitation. *Int. J. Climatol.*, **35**, 1465–1483, https://doi.org/10.1002/joc.4069.

Mass, C., 2024: Implementation of IFS cycle 48r1. ECMWF, accessed 25 August 2024, https://confluence.ecmwf.int/display/FCST/Implementation+of+IFS+Cycle+48r1.

Magnusson, L., and Coauthors, 2022: Skill of medium-range forecast models using the same initial conditions. *Bull. Amer. Meteor. Soc.*, **103**, E2050–E2068, https://doi.org/10.1175/BAMS-D-21-0234.1.

Mantripragada, R. S. S., C. J. Schreck, and A. Aiyyer, 2021: Energetics of interactions between African easterly waves and convectively coupled Kelvin waves. *Mon. Wea. Rev.*, **149**, 3821–3835, https://doi.org/10.1175/mwr-d-21-0003.1.

Matsuno, T., 1966: Quasi-geostrophic motions in the equatorial area. *J. Meteor. Soc. Japan*, **44**, 25–43, https://doi.org/10.2151/jmsj1965.44.1_25.

Mayta, V. C., and A. F. Adames, 2023: Moist thermodynamics of convectively coupled waves over the Western Hemisphere. *J. Climate*, **36**, 2765–2780, https://doi.org/10.1175/JCLI-D-22-0435.1.

——, G. N. Kiladis, J. Dias, P. L. Silva Dias, and M. Gehne, 2021: Convectively coupled Kelvin waves over tropical South America. *J. Climate*, **34**, 6531–6547, https://doi.org/10.1175/JCLI-D-20-0662.1.

Mekonnen, A., C. D. Thorncroft, A. R. Aiyyer, and G. N. Kiladis, 2008: Convectively coupled Kelvin waves over tropical Africa during the boreal summer: Structure and variability. *J. Climate*, **21**, 6649–6667, https://doi.org/10.1175/2008JCLI2008.1.

Moron, V., A. W. Robertson, M. N. Ward, and O. Ndiaye, 2008: Weather types and rainfall over Senegal. Part I: Observational analysis. *J. Climate*, **21**, 266–287, https://doi.org/10.1175/2007JCLI1601.1.

Mounier, F., G. N. Kiladis, and S. Janicot, 2007: Analysis of the dominant mode of convectively coupled Kelvin waves in the West African monsoon. *J. Climate*, **20**, 1487–1503, https://doi.org/10.1175/JCLI4059.1.

Pathak, J., and Coauthors, 2022: FourCastNet: A global data-driven high-resolution weather model using adaptive Fourier neural operators. arXiv, 2202.11214v1, https://doi.org/10.48550/ARXIV.2202.11214.

Peyrillé, P., R. Roehrig, and S. Sanogo, 2023: Tropical waves are key drivers of extreme precipitation events in the Central Sahel. *Geophys. Res. Lett.*, **50**, e2023GL103715, https://doi.org/10.1029/2023GL103715.

Reed, R. J., A. Hollingsworth, W. A. Heckley, and F. Delsol, 1988: An evaluation of the performance of the ECMWF operational system in analyzing and forecasting easterly wave disturbances over Africa and the tropical Atlantic. *Mon. Wea. Rev.*, **116**, 824–865, https://doi.org/10.1175/1520-0493(1988)116<0824:AEOTPO>2.0.CO;2.

Rios-Berrios, R., F. Judt, G. Bryan, B. Medeiros, and W. Wang, 2023: Three-dimensional structure of convectively coupled equatorial waves in aquaplanet experiments with resolved or parameterized convection. *J. Climate*, **36**, 2895–2915, https://doi.org/10.1175/JCLI-D-22-0422.1.

——, B. H. Tang, C. A. Davis, and J. Martinez, 2024: Modulation of tropical cyclogenesis by convectively coupled Kelvin waves. *Mon. Wea. Rev.*, **152**, 2309–2322, https://doi.org/10.1175/MWR-D-24-0052.1.

Russell, J. O., A. Aiyyer, J. D. White, and W. Hannah, 2017: Revisiting the connection between African easterly waves and Atlantic tropical cyclogenesis. *Geophys. Res. Lett.*, **44**, 587–595, https://doi.org/10.1002/2016GL071236.

Ryglicki, D. R., and R. E. Hart, 2015: An investigation of center-finding techniques for tropical cyclones in mesoscale models. *J. Appl. Meteor. Climatol.*, **54**, 825–846, https://doi.org/10.1175/JAMC-D-14-0106.1.

Schlueter, A., A. H. Fink, P. Knippertz, and P. Vogel, 2019: A systematic comparison of tropical waves over Northern Africa. Part I: Influence on rainfall. *J. Climate*, **32**, 1501–1523, https://doi.org/10.1175/JCLI-D-18-0173.1.

Schreck, C. J., 2015: Kelvin waves and tropical cyclogenesis: A global survey. *Mon. Wea. Rev.*, **143**, 3996–4011, https://doi.org/10.1175/MWR-D-15-0111.1.

——, M. A. Janiga, and S. Baxter, 2020: Sources of tropical subseasonal skill in the CFSv2. *Mon. Wea. Rev.*, **148**, 1553–1565, https://doi.org/10.1175/MWR-D-19-0289.1.

Torn, R. D., 2010: Ensemble-based sensitivity analysis applied to African easterly waves. *Wea. Forecasting*, **25**, 61–78, https://doi.org/10.1175/2009WAF2222255.1.

Torres, V. M., C. D. Thorncroft, and N. M. J. Hall, 2021: Genesis of easterly waves over the tropical eastern Pacific and the intra-Americas sea. *J. Atmos. Sci.*, **78**, 3263–3279, https://doi.org/10.1175/JAS-D-20-0389.1.

Vargas Martes, R. M., A. F. Adames Corraliza, and V. C. Mayta, 2023: The role of water vapor and temperature in the thermodynamics of tropical northeast Pacific and African easterly waves. *J. Atmos. Sci.*, **80**, 2305–2322, https://doi.org/10.1175/JAS-D-22-0177.1.

Weber, N. J., D. Kim, and C. F. Mass, 2021: Convection–Kelvin wave coupling in a global convection-permitting model. *J. Atmos. Sci.*, **78**, 1039–1055, https://doi.org/10.1175/JAS-D-20-0243.1.

Wheeler, M., and G. N. Kiladis, 1999: Convectively coupled equatorial waves: Analysis of clouds and temperature in the wavenumber–frequency domain. *J. Atmos. Sci.*, **56**, 374–399, https://doi.org/10.1175/1520-0469(1999)056<0374:CCEWAO>2.0.CO;2.

Wolding, B., J. Dias, G. Kiladis, F. Ahmed, S. W. Powell, E. Maloney, and M. Branson, 2020a: Interactions between moisture and tropical convection. Part I: The coevolution of moisture and convection. *J. Atmos. Sci.*, **77**, 1783–1799, https://doi.org/10.1175/JAS-D-19-0225.1.

——, ——, ——, E. Maloney, and M. Branson, 2020b: Interactions between moisture and tropical convection. Part II: The convective coupling of equatorial waves. *J. Atmos. Sci.*, **77**, 1801–1819, https://doi.org/10.1175/JAS-D-19-0226.1.

Yang, G.-Y., B. Hoskins, and J. Slingo, 2003: Convectively coupled equatorial waves: A new methodology for identifying wave structures in observational data. *J. Atmos. Sci.*, **60**, 1637–1654, https://doi.org/10.1175/1520-0469(2003)060<1637:CCEWAN>2.0.CO;2.

——, ——, and ——, 2007a: Convectively coupled equatorial waves. Part I: Horizontal and vertical structures. *J. Atmos. Sci.*, **64**, 3406–3423, https://doi.org/10.1175/JAS4017.1.

——, ——, and ——, 2007b: Convectively coupled equatorial waves. Part II: Propagation characteristics. *J. Atmos. Sci.*, **64**, 3424–3437, https://doi.org/10.1175/JAS4018.1.

——, J. Slingo, and B. Hoskins, 2009: Convectively coupled equatorial waves in high-resolution Hadley Centre climate models. *J. Climate*, **22**, 1897–1919, https://doi.org/10.1175/2008JCLI2630.1.

——, S. Ferrett, S. Woolnough, J. Methven, and C. Holloway, 2021: Real-time identification of equatorial waves and evaluation of waves in global forecasts. *Wea. Forecasting*, **36**, 171–193, https://doi.org/10.1175/WAF-D-20-0144.1.